Atmos. Chem. Phys. Discuss., doi:10.5194/acp-2017-64, 2017
Manuscript under review for journal Atmos. Chem. Phys.
Published: 1 February 2017

Atmospheric Chemistry and Physics Discussions

Vertical distribution of the phase state of particles in tropical deep-convective clouds as derived from cloud-side reflected solar radiation measurements

Evelyn Jäkel[1], Manfred Wendisch[1], Trisomono C. Krisna[1], Florian Ewald[2,3], Tobias Kölling[2], Tina Jurkat[3], Christiane Voigt[3], Micael A. Cecchini[4], Luiz A. T. Machado[4], Armin Afchine[5], Anja Costa[5], Martina Krämer[5], Meinrat O. Andreae[6,7], Ulrich Pöschl[6], Daniel Rosenfeld[8], and Tianle Yuan[9]

[1]Leipzig Institute for Meteorology (LIM), University of Leipzig, Germany.
[2]Meteorological Institute, Ludwig-Maximilians-University Munich, Germany.
[3]Institut für Physik der Atmosphäre, Deutsches Zentrum für Luft und Raumfahrt (DLR), Oberpfaffenhofen, Germany.
[4]Center of Weather Forecast and Climates Studies (CPTEC), National Institute for Space Research (INPE), Sao Jose Dos Campos, Brazil.
[5]Forschungszentrum Jülich, Jülich, Germany.
[6]Max Planck Institute for Chemistry (MPIC), Mainz, Germany.
[7]Scripps institution of Oceanography, University of California San Diego, La Jolla, California, USA.
[8]Institute of Earth Sciences, The Hebrew University of Jerusalem, Jerusalem, Israel.
[9]NASA Goddard Space Flight Center, Greenbelt, Maryland, USA.

Correspondence to: E. Jäkel
e.jaekel@uni-leipzig.de

Abstract. Vertical profiles of the cloud particle phase state in tropical deep-convective clouds (DCCs) were investigated using airborne solar radiation data collected by the German research aircraft HALO during the ACRIDICON-CHUVA campaign, which was conducted over the Brazilian Amazon in September 2014. A phase discrimination retrieval based on imaging spectroradiometer measurements of cloud side spectral reflectivity was applied to DCCs under different aerosol conditions. From the retrieval results the height of the mixed phase layer of the DCCs was determined. The retrieved profiles were compared with in situ measurements and satellite observations. It was found that the depth and vertical position of the mixed phase layer can vary up to 900 m for one single cloud scene. In particular, this variation is attributed to the different stages of cloud development in one scene. Clouds of mature or decaying stage are affected by falling ice particles resulting in lower levels of fully glaciated cloud layers compared to growing clouds. Comparing polluted and moderate aerosol conditions revealed a shift of the lower boundary of the mixed phase layer from 5.6±0.2 km (269 K) [moderate] to 6.2±0.3 km (267 K) [polluted], and of the upper boundary from 6.8±0.2 km (263 K) [moderate] to 7.4±0.4 km (259 K) [polluted], as would be expected from theory.

Atmos. Chem. Phys. Discuss., doi:10.5194/acp-2017-64, 2017
Manuscript under review for journal Atmos. Chem. Phys.
Published: 1 February 2017

Atmospheric Chemistry and Physics Discussions

1 Introduction

Deep-convective clouds (DCCs) play a crucial role in redistributing latent heat, influencing the hydrological cycle, and regulating the radiative energy budget of the Earth's climate system. In particular, tropical convection is a key component of the global circulation of the atmosphere, which is the primary pathway for energy transport from the tropics to the mid-latitudes. DCCs exhibit a highly complex vertical microphysical structure, including different phase states of water (liquid, mixed phase, and ice) and a high variability of cloud particle sizes. The optical, microphysical, and macrophysical properties of DCCs determine their radiative effects and are controlled by particle growth processes occurring within the clouds.

Consequently, the understanding of the processes driving the evolution of DCCs is of major importance. In particular, aerosol particles modify cloud properties, including their radiative effects (Twomey, 1977), as well as their lifetime and the formation of precipitation (Albrecht, 1989). Many efforts have been undertaken to quantify these effects and processes, which take place over a wide range of spatial and temporal scales (Rosenfeld et al., 2014). Aerosol particles have an influence on the cloud droplet size distributions (more aerosols particles lead to more and smaller cloud droplets), on warm rain and cold rain development, on the cloud top height evolution, the depth of the mixed phase layer, and the occurrence of lightning (Tao et al., 2012). While the formation of warm-rain is suppressed by enhanced aerosol particle number concentration, the cold-rain evolution is intensified due to extra latent heat, which leads to an invigoration of the DCC development (Andreae et al., 2004; Rosenfeld et al., 2008).

In particular, the phase transition from liquid water to ice is relevant for the development of precipitation. Furthermore, the optical properties of ice and liquid water clouds differ and thus cause different radiative effects. Rosenfeld and Lensky (1998) found that in continental clouds glaciation occurs at much colder temperatures (-15° C to -30° C) than in maritime clouds (warmer than -10° C). Consequently, the vertical transitional mixed phase zone in continental clouds is geometrically thicker than in maritime clouds. In polluted clouds the coalescence zone vanishes (in which droplet growth by collision and coalescence play a major role), and mostly small liquid water droplets are observed. The mixed phase zone is shifted to lower temperatures (less than -15°C), and glaciation occurs often above the -30°C isotherm, with the extreme situation of polluted clouds with strong updrafts reaching to -38°C (Rosenfeld and Woodley, 2000).

Profile measurements of microphysical structure and formation of precipitation remains a challenge. Either in situ measurements (Freud et al., 2008; Konwar et al., 2012; Khain et al., 2013, e.g.,) or remote sensing techniques are applied to obtain profiles of cloud microphysical parameters, such as cloud particle size and phase state. Active remote sensing measurements (e.g., radar) provide profiles along the line-of-sight. These sensors may penetrate through a cloud, but the quantitative retrieval of cloud optical and microphysical properties is problematic since the signal is dominated by scattering due to large droplets.

Rosenfeld and Lensky (1998) introduced a method to derive vertical profiles of the effective droplet radius as a function of brightness temperature from satellite reflectance measurements. They analyzed clusters of convective clouds at different stages of vertical development to retrieve the temporal evolution of individual cloud elements. This ensemble method assumes that cloud-top properties derived from clouds at different stages of their evolution are similar to the properties of a single cloud as it grows through the various heights (Freud et al., 2008). Rosenfeld et al. (2014) have shown an improved detection of cloud

Atmos. Chem. Phys. Discuss., doi:10.5194/acp-2017-64, 2017
Manuscript under review for journal Atmos. Chem. Phys.
Published: 1 February 2017

Atmospheric Chemistry and Physics Discussions

microphysical processes for the 375-m resolution data of the NPP/VIIRS (National Polar-orbiting Partnership/Visible Infrared Imaging Radiometer Suite) compared to the standard 1-km resolution data of MODIS (Moderate Resolution Imaging Spectroradiometer). Small scale convective cloud elements are better resolved with higher spatial resolution by the NPP/VIIRS, whereas MODIS retrievals [based on one-dimensional (1D) radiative transfer simulations] are biased by the plane-parallel assumptions (Cahalan, 1994). A decrease of pixel size causes an increase of the independent pixel bias because the smaller the pixel, the more important is the net horizontal photon transport. The retrieval uncertainty due to the 1D approximation and the assumptions made with respect to the ensemble method can be mitigated by using multi-angle spectroradiometer measurements (ground-based, airborne, or satellite) of cloud side spectral reflectivity to derive vertical profiles of microphysical cloud parameters. A step further is the application of high-resolution imaging spectroradiometers, which offer a profiling of individual clouds with a temporal resolution of one minute from both ground or aircraft. For airborne applications there are no safety-related flight restrictions due to strong turbulences and icing as would be required in case of cloud penetrations for in situ probing.

The retrieval of the thermodynamic water phase based on cloud side observations exploits the differences in the imaginary part of the refractive index of the cloud particles of both phases in the near infrared (NIR: 0.7-2.5 μm) wavelength range (Pilewskie and Twomey, 1987; Ehrlich et al., 2008; Martins et al., 2011; Jäkel et al., 2013). While Pilewskie and Twomey (1987) and Jäkel et al. (2013) applied ground-based measurements of spectral reflectivity between 1.5 – 1.7 μm wavelength for the phase discrimination, Martins et al. (2011) utilized reflected radiation data at 2.10 μm and 2.25 μm wavelength. A phase index was defined by Jäkel et al. (2013) using the spectral slope of cloud side reflected radiances between 1.55 and 1.7 μm. They showed by applying 3D radiative transfer simulations that this slope is negative for liquid water and positive for ice particles, mostly independent of the viewing geometry and cloud particles size. For DCCs with liquid water, ice particles, and mixed phase layers, profile measurements of the phase index provide evidence where and in which stage of development ice particles start to form. For ground-based observations, Jäkel et al. (2013) identified the mixed phase zone by a strong increase of the phase index from negative to positive values, while the vertical profile of the phase index for pure liquid water or ice particles is less variable.

To determine the height and temperature of the mixed phase layer from cloud side spectral reflectivity observations additional information is required. Martins et al. (2011) used a thermal infrared sensor at 11 μm wavelength yielding the brightness temperature, which is an indicator of cloud height. Collocated scanning active remote sensing techniques by radar or lidar were applied to estimate geometric information on cloud distance and height (Jäkel et al., 2013; Ewald et al., 2015). Another method is based on stereographic analysis of multiangle observations (e.g., Seiz and Davies, 2006).

In further development of the scanning, point-sensor measurements as presented by Martins et al. (2011), this paper introduces airborne measurements of an imaging spectroradiometer called specMACS (spectrometer of the Munich Aerosol Cloud Scanner, Ewald et al., 2016) to characterize vertical profiles of the phase state of DCCs as observed during the HALO (High Altitude and Long Range Research Aircraft) campaign ACRIDICON (Aerosol, Cloud, Precipitation, and Radiation Interactions and Dynamics of Convective Cloud Systems) - CHUVA (Cloud processes of tHe main precipitation systems in Brazil: A contribUtion to cloud resolVing modeling and to the GPM (GlobAl Precipitation Measurement)) in 2014 (Wendisch et al.,

Atmos. Chem. Phys. Discuss., doi:10.5194/acp-2017-64, 2017
Manuscript under review for journal Atmos. Chem. Phys.
Published: 1 February 2017

Atmospheric Chemistry and Physics Discussions

2016). The measurement technique of imaging spectroradiometers allows instantaneous spectral cloud side observations for a set of viewing angles depending on the number of spatial pixels of the sensor. The imaging spectroradiometer measurements were supplemented by GoPro camera observations to estimate the cloud distance and height from stereographic analysis of the additional video camera data. The instrumentation and the field campaign are introduced in Section 1, followed by a description of the methodology of the phase retrieval (Sec. 2). In Section 3 the method is applied to data from three flights during ACRIDICON-CHUVA and compared to in situ and MODIS products.

2 Measurements and tools

2.1 Field campaign

Remote sensing and in situ data sampled during ACRIDICON-CHUVA are used to derive vertical profiles of the thermodynamic water phase of cloud particles in DCCs as measured over the Brazilian rainforest. Local convection is strongly forced by the diurnal cycle. In particular, at the end of the dry season (September) a large variability of aerosol particles due to biomass burning is observed (Andreae et al., 2015). Three out of fourteen scientific flights were selected for this study (flight tracks shown in Fig. 1) covering an area of about 1400 x 1200 km^2. The temperature profiles of the three flights show only small day–to–day variations in spite of the different flight directions. In the overview paper of the ACRIDICON-CHUVA campaign by Wendisch et al. (2016) the aerosol conditions from AC13 was classified as polluted. Cecchini et al. (2017) used the aerosol concentration measured with a condensation particle counter (CPC) at cloud base for flights AC13 and AC18 as indicator. They found 4100 particles cm^{-3} for AC13 suggesting polluted clouds and about 740 particles cm^{-3} for AC18 indicating clouds under Amazonian background conditions typical of the dry season. No appropriate measurements at cloud base were available for AC10. Ground-based measurements on this day at the Amazonian Tall Tower Observatory (ATTO) located at -2.143◦S and -59.001◦W revealed a particle concentration between 1100 and 1600 cm^{-3}. Since the flight AC10 was in the same general region, these data are used to describe the aerosol condition of AC10. Furthermore, the aerosol optical depth in the main measurement areas taken from MODIS product MOD04/MYD04 (3-km-pixel resolution) was chosen as additional parameter. Quite variable values between 0.3-0.4 for AC18 (28 September 2014), between 0.4-0.5 for AC10 (12 September 2014) and between 0.5-0.6 for AC13 (19 September 2014) were found. From these data AC10 and AC18 were classified as moderate aerosol cases.

2.2 Instrumentation

2.2.1 specMACS and GoPro

The imaging spectroradiometer specMACS (Ewald et al., 2016) consists of two line cameras (manufactured by SPECIM, Finland), one for the visible and near-infrared (VNIR), the other for the shortwave infrared (SWIR) spectral range. The field of view (FOV) along the spatial lines of both cameras differs slightly (33° and 35°) due to different optics. The incoming solar radiation is distributed over 1312 and 320 spatial pixels, respectively. For each spatial pixel, spectral information can be

Atmos. Chem. Phys. Discuss., doi:10.5194/acp-2017-64, 2017
Manuscript under review for journal Atmos. Chem. Phys.
Published: 1 February 2017

Atmospheric Chemistry and Physics Discussions

measured within 0.4 – 1.0 μm (800 spectral channels) and 1.0 – 2.5 μm (256 spectral channels), respectively, with a spectral bandwidth between 2.5 – 12.0 nm.

The measurement system was characterized in the laboratory with respect to nonlinearity, dark current, and polarization (Ewald et al., 2016). Spatial calibrations were performed to derive the angular resolution of both sensors, which is needed for final geometric matching of both sensors. The spectral characteristics were deduced by measuring monochromatic radiation from a monochromator. The absolute radiometric response was determined using an integrating sphere and the absolute RAdiance STAndard (RASTA; Schwarzmaier et al., 2012) traceable to absolute radiance standards of PTB (Physical Technical Bundesanstalt). Finally, wavelength-dependent uncertainties (2σ) of the absolute radiometric response including sensor noise and dark current drift between 3% and 14% (in the outer region of the measured spectra) were given in Ewald et al. (2016).

During the ACRIDICON-CHUVA campaign, specMACS was mounted at the side view port on HALO. The transmission of the optical window with purified quartz glass panes (type: Herasil 102) was characterized in the laboratory. The line cameras were orientated in vertical position as illustrated in Fig. 2. During the aircraft movement 3D (two spatial, one spectral dimension) snapshots of cloud scenes were taken.

For estimates of the cloud distance a 2D digital action camera (type: Hero HD3+ 3660-023 Full-HD manufactured by GoPro, Inc., USA, and hereafter called GoPro) was installed at the side window of HALO. Movies with full HD at a resolution of 1920 x 1080 pixels were recorded during the flight. The original lens of the camera was replaced by a distortion free optics covering a horizontal FOV_h of about 90° and a vertical FOV_v of about 59°. A schematic of the setup is shown in Fig. 2. The geometrical calibration of the camera was performed using a square chessboard. Images from different perspectives of the chessboard were taken and evaluated by an open source routine (http://opencv.org) implemented in computer vision algorithms (Bradski and Kaehler, 2013). This allows allocating elevation and azimuthal angle to each point of the image.

2.2.2 MODIS

MODIS cloud products of the Terra (MOD06) and Aqua (MYD06) satellites have been used in this study for a comparison of the phase state and glaciation temperature. Since MODIS mainly measures cloud top properties, the time–space–exchangeability of convective clouds as proposed by Rosenfeld and Lensky (1998) is applied. The cloud particle phase is directly taken from the MOD06/MYD06 product "Cloud_Phase_Infrared" with a 1-km-pixel resolution (Platnick et al., 2003). The estimation of the glaciation temperature is based on the retrieval presented by Yuan et al. (2010). The vertical distribution and evolution of cloud particle size inside a DCC provides useful information on the phase state (Rosenfeld and Feingold, 2003). The mixed phase layer is characterized by a strong increase of cloud particle size with height, whereas for fully glaciated cloud layers the largest ice particles can be found directly at the height where the glaciation temperature is reached. At lower temperatures, no supercooled droplets are left for particle growth and only small ice particles are able to move upward inside weakened updrafts. Consequently, the height and temperature where the increase of particle size turns into a decrease is considered as glaciation level and temperature. A sufficiently large statistics is required for the ensemble method. The cloud particle sizes from the MOD06/MYD06 product are averaged for a bin of cloud brightness temperatures (Channel 31; 11 μm).

Atmos. Chem. Phys. Discuss., doi:10.5194/acp-2017-64, 2017
Manuscript under review for journal Atmos. Chem. Phys.
Published: 1 February 2017

Atmospheric Chemistry and Physics Discussions

In contrast to the original retrieval (Yuan et al., 2010), the restrictions concerning cloud optical depth (COD $>$ 30) and cloud top temperature (CTT $<$ 260 K) were relaxed to COD $>$ 10 and CTT $<$ 280 K, to enlarge the statistics of the data.

2.2.3 NIXE-CAPS

In situ measurements of the asphericity of particles were performed with the Novel Ice eXpEriment – Cloud, Aerosol and Precipitation Spectrometer (NIXE-CAPS). The instrument is a combination of two probes, the NIXE-CAS (Cloud and Aerosol Spectrometer) and the NIXE-CIP (Cloud Imaging Probe). While the NIXE-CIP detects the size of particles between 15 and 900 μm by recording 2-D shadow cast images, the NIXE-CAS measures the size and asphericity of the particles for a range of 0.6 and 50 μm (Meyer, 2012; Luebke et al., 2016). NIXE-CAS discriminates between spherical and aspherical particles by measuring the change of the polarized components of the scattered laser light in the backward direction which is sensitive to the particle shape. Spherical particles do not strongly alter the polarization state of the incident light, while non-spherical ice crystals change the polarization depending on the their size and orientation (Nicolet et al., 2007). With respect to the phase state classification, aspherical particles can be considered as ice particles. In contrast, spherical particles indicate mainly liquid droplets. Note, that while Järvinen et al. (2016) have shown that ice particles can also be spherical, the large majority of spherical particles is associated with the liquid phase. The ACRIDCON-CHUVA data set was classified with respect to temperature, asphericity, and particle number concentration as measured by NIXE-CAPS (see Table 1).

2.2.4 CAS-DPOL and LWC hotwire

The CAS-DPOL (Cloud and Aerosol Spectrometer, with detector for polarization) instrument measures aerosol and cloud particles in the size range between 0.5 and 50.0 μm (Braga et al., 2016; Voigt et al., 2016) by sensing individual particles passing a focused laser beam. The resulting intensity distribution of forward and backward scattered light is used to derive the size distribution of the particles. Here, only particles with diameters between 3 and 50 μm and with a total number density larger than 1 cm^{-3} are classified. Additionally, CAS-DPOL is used to estimate the phase of the cloud particles (liquid or ice). The aspherical fraction (AF) is determined by a size dependent ratio of the polarized backward scattered and the forward scattered light. The aspherical fraction is the ratio of aspherical particles and the sum of all detected particles. Calibration of the backward channel was performed during RICE03 (Rough ICE campaign) at the AIDA (Aerosol Interactions and Dynamics in the Atmosphere) cloud chamber (Järvinen et al., 2016; Schnaiter et al., 2016). Spherical liquid particles reveal a low AF ($<$ 0.1) while aspherical particles (ice or aerosols) have a high AF ($>$ 0.1, mean of 0.4). Aspherical ice particles may have an AF $<$ 1 since the orientation of the particles in the sampling volume may appear circular.

The liquid water content (LWC) is measured with a King type LWC Hotwire (Braga et al., 2016) installed on the CAS-DPOL. Only data above a conservative detection limit of 0.3 g m^{-3} is used.

Atmos. Chem. Phys. Discuss., doi:10.5194/acp-2017-64, 2017
Manuscript under review for journal Atmos. Chem. Phys.
Published: 1 February 2017

Atmospheric Chemistry and Physics Discussions

2.3 Radiative transfer model

3D radiative transfer modeling is performed with the forward-propagating Monte Carlo photon-transport model MCARATS (Monte Carlo Atmospheric Radiative Transfer Simulator) (Iwabuchi, 2006). The optical properties (single scattering albedo, extinction coefficient, and phase function) of atmospheric components are pre-defined by the user for each grid cell of the model domain as either horizontally inhomogeneous or homogeneous layers. Profiles of temperature, atmospheric pressure, density, and gases taken from Anderson et al. (1986) have been adjusted by a radio sounding from Alta Floresta (-9.866°S, -56.105°W) and profile measurements of temperature, humidity and pressure performed by the HALO aircraft to represent the atmospheric conditions on 19 September 2014 (AC13) in the region of one of the measurement flights (representative of the three flights considered in this study). Since Rayleigh scattering is calculated from the density profile according to Bodhaine et al. (1999), the LOWTRAN (Low Resolution Transmission Model) parametrization by Pierluissi and Peng (1985), as adapted from SBDART (Santa Barbara DISORT Atmospheric Radiative Transfer) (Ricchiazzi and Gautier, 1998) is used for gas absorption. The optical properties of clouds are derived from profiles of effective radius (r_{eff}) and liquid (ice) water content (LWC, IWC) using Mie calculations for water clouds, while for ice clouds the parameterizations by Baum et al. (2005, 2007) were used. For the polluted aerosol case, aerosol properties were described with the model by Shettle (1989) and adjusted by AERONET (AErosol RObotic NETwork) measurements (site Alta Floresta) of aerosol optical depth, single scattering albedo, and asymmetry parameter (used for the Henyey-Greenstein phase function).

3 Methodology

The retrieval method of the phase state consists of three main steps: (3.1) The cloud masking procedure to filter illuminated cloud regions, (3.2) the cloud phase discrimination, and (3.3) the geometric allocation of the classified cloud profiles with respect to height and temperature.

3.1 Cloud masking procedure

Since the spectral signature of reflected radiation from shadowed regions of cloud sides is contaminated by a significant fraction of diffuse radiation originating from unknown cloud regions, a cloud masking technique was developed to discriminate illuminated and shadowed cloud regions. In ground-based observations the reflected radiation measured from shadowed cloud regions showed spectral signatures influenced by the spectral surface albedo due to interaction between clouds and the surface (Jäkel et al., 2013). However, for airborne measurements such spectral indication could neither be observed nor simulated because of a different viewing geometry. Therefore, a different approach was chosen based on the distribution of color values in the observed cloud scene. Three wavelengths (λ_{B} = 436 nm, λ_{G} = 555 nm, and λ_{R} = 700 nm) corresponding to wavelengths of the RGB (Red Green Blue) color space are selected to calculate a simplified RGB color value for each measured spectrum, which takes into account the sensitivity of the human eye on the different colors by differential weighting of the three

Atmos. Chem. Phys. Discuss., doi:10.5194/acp-2017-64, 2017
Manuscript under review for journal Atmos. Chem. Phys.
Published: 1 February 2017

Atmospheric Chemistry and Physics Discussions

wavelengths:

$$\mathrm{RGB} = 0.2126 \cdot \mathrm{R} + 0.7152 \cdot \mathrm{G} + 0.0722 \cdot \mathrm{B} \quad (1)$$

where R, G, and B represent the normalized spectral radiances.

In a next step the histogram of the RGB values for the observed cloud scene is evaluated with respect to distinctive modes in the frequency distribution, indicating illuminating and shadowed cloud areas. The procedure is illustrated using simulated cloud side reflectivity observations for a cloud field that was generated by the Goddard Cumulus Ensemble model (Tao et al., 2003; Zinner et al., 2008) for a model domain of 64 x 64 km with a horizontal resolution of 250 m. The maximum extension of the liquid water clouds from bottom to cloud top ranges from 1.0 to 7.4 km altitude. As MCARATS is a forward-propagating radiative transfer model (RTM) the simulations were performed for each grid point representing an observation altitude of 4 km. The sensor is pointed at an elevation angle of 10° and with a relative azimuth angle to the sun of 60° to trigger also areas of shadowed clouds. Fig. 3a displays the RGB color values derived from the radiance simulations at each of the 256 x 256 grid points. From information of the viewing geometry of the sensor and Sun (solar zenith angle θ_0 = 30°) and the setup of the clouds in the model domain, each observed cloud pixel was classified as shadowed or illuminated. The histogram of the simulated RGB color values for all cloud observations is shown in Fig. 3b as black line. Two modes are visible, which coincide with the two sub-classes of illuminated and shadowed cloud regions. To identify the illuminated cloud areas for an unknown cloud geometry, as is the case for real measurements, only the brightest pixels that correspond to the right-most mode in the RGB-histogram are selected. Since the left side of this mode may also include data from shadowed regions, data larger than the maximum of this mode will be classified as illuminated and used for the cloud phase retrieval. Fig. 3c illustrates the RGB histogram for a cloud scene measured during ACRIDICON-CHUVA from 19 September 2014.

The relative azimuth angle between the sun and the viewing direction of specMACS was 68° with θ_0 = 39°. The selected cloud scene was observed with an elevation ranging between -13 and +12°. The inlay in Fig. 3c shows the cloud situation as observed from specMACS. Applying the threshold criteria to identify the illuminated cloud parts gives a cloud mask as presented in Fig. 3d, where the illuminated cloud parts are highlighted.

3.2 Cloud phase discrimination

Vertical profiles of the relationship between temperature and particle size to identify the mixed phase cloud layer have been used by e.g., Rosenfeld and Woodley (2003). For continental conditions (as often observed in the Amazon Basin) the droplet size may not significantly increase between the main coalescence and mixed phase regions. Therefore, for these cases it is difficult to define the height or temperature where phase transition takes place by the increase of the droplet size. As presented in Ehrlich et al. (2008), Jäkel et al. (2013), and Jäkel et al. (2016), another method based on differences of the refractive index of ice and liquid water between 1550 and 1700 nm wavelength can be applied to discriminate the thermodynamic water phase. The so-called phase index I_P based on spectral radiances (I) was introduced as:

$$I_\mathrm{P} = \frac{I_{1700} - I_{1550}}{I_{1700}} \quad . \quad (2)$$

Atmos. Chem. Phys. Discuss., doi:10.5194/acp-2017-64, 2017
Manuscript under review for journal Atmos. Chem. Phys.
Published: 1 February 2017

Atmospheric Chemistry and Physics Discussions

A change of the gradient in the profile of the phase index was observed in simulated cloud side observations between liquid water and mixed phase, and mixed phase and ice phase, respectively. Similar simulations as in Jäkel et al. (2013) using MCARATS were performed for atmospheric conditions during ACRIDICON-CHUVA on 19 September 2014. The model domain has 140 x 40 x 99 grid cells with a horizontal resolution of 250 m and a vertical resolution of 200 m below 14 km altitude and variable resolution above. For each grid cell in a flight altitude of 8 km the spectral radiance at 1550 and 1700 nm wavelength is simulated for sensor viewing elevation angles between -20 and +20° corresponding to the FOV of specMACS. The simulations are performed for two artificial clouds ranging between 4.0 and 11.0 km altitude with a mixed phase layer between 6.4 and 7.0 km. For the first cloud case, particles with constant effective radius (r_{eff} = 20 μm for liquid water and ice and constant water content of 0.7 gm^{-3} are assumed. For each horizontal cloud distance between 3 and 8 km, a profile of the phase index was determined in 250 m steps. The combined I_{P}-profile is plotted in Fig. 4a in black dots. Due to the variation of cloud distance and viewing elevation angle, the I_{P}-profile comprises reflected radiances originated from various scattering angles. Three distinct clusters corresponding to the three phase states of water, with negative values for pure liquid water, can be found. The phase index is significantly shifted to positive values with some variability for the mixed phase layer. The difference of the phase index between mixed and ice phase is less pronounced than between liquid and mixed phase. Obviously the contribution of ice particles within the mixed phase layer leads to a pronounced absorption resulting in an increase of the phase index. The variability of the phase index for constant microphysical conditions in each of the three phases is caused by the effect of the different viewing geometries. Each cloud height is observed from different sensor elevation angles and distances. As the scattering phase function depends on the scattering angle, the wavelength and the particle shape, the viewing geometry of the sensor related to the position of the sun (here: θ_0 = 30°) also modulate the phase index. Therefore, a direct conclusion on the particle size with a priori knowledge of the phase state can only be drawn when also the geometry of the observed cloud is known. For more realistic clouds, the size of ice particles is larger than the size of liquid particles, which is taken into account in the second case with variable cloud microphysical properties. The corresponding vertical profile of the effective radius and the water content of the cloud is plotted in Fig. 4b. The mixed phase layer is characterized by the maximum particle sizes of liquid and ice particles over the entire profile, but lower water content compared to regions above and below. As concluded in Jäkel et al. (2013), the phase index gets less variable for a water content of more than 0.4 gm^{-3} (variation lower than 7 %) which is away from the edges of DCCs. Consequently, mainly the particle size and the phase state drive the changes of the phase index with height. Less impact is attributable to the change of the sensor elevation angle, as can be concluded from the comparison between the two cloud cases. The variability of the phase index with respect to the viewing geometry for each phase state in the first cloud case with fixed cloud microphysics is lower than the variability of I_{P} due to the changed cloud properties in the second cloud case. In particular, the mixed phase layer for the second case is characterized by a significant increase of the phase index with height. Once the pure ice phase is reached, the slope of I_{P} decreases. In the following, the magnitude of vertical change of the phase index will serve as indicator of the position of the mixed phase layer.

Atmos. Chem. Phys. Discuss., doi:10.5194/acp-2017-64, 2017
Manuscript under review for journal Atmos. Chem. Phys.
Published: 1 February 2017

Atmospheric Chemistry and Physics Discussions

3.3 Cloud geometry retrieval

Due to the spatial dimension of the specMACS-SWIR instrument, reflected radiances are measured for 320 different angles with an average pixel-to-pixel spacing of about 0.11°. To quantify the vertical position of the mixed phase layer in terms of height or temperature, information on the cloud distance needs to be gathered by independent measurements. For that purpose, collocated images of the GoPro camera are combined with flight attitude data to apply stereo-photogrammetric methods. The theoretical background on this method is given in Hartley and Zisserman (2004), while exemplarily Hu et al. (2009) applied these techniques for cloud geometrical reconstruction. Basically, to estimate the distance to the observed cloud element (C) two images from different positions (P1 and P2) showing a projection of the observed point in both images (C1 and C2, so-called tie points) need to be taken (see Fig. 5a). The point C and the two camera centers P1 and P2 define the epipolar plane. The images C1 and C2 of C in the two images lie on this plane. In fact, the geometric problem comprises three different coordinate systems, one for the camera, one for the aircraft, and the world coordinate system for the observed point C. Therefore, coordinate transformations are required to relate the different coordinate systems. Fig. 5b illustrates the aircraft and camera coordinate system which differ because the GoPro camera looks perpendicular to the flight direction. Exemplarily, a positive pitch angle of the aircraft rotates the camera (image) around the camera's x-axis. The x -and y-axis of the world coordinate system (not shown) are pointed to the east and to the north, respectively, while the z-axis is perpendicular to the x-y plane (pointing upward). Each selected image in the camera system (x_i, y_i, z_i) is transformed into the aircraft coordinate system (x_a, y_a, z_a), and finally into the world system (x_w, y_w, z_w). This transformation requires the rotation of the coordinate systems with respect to the three Euler angles pitch, roll, and yaw using the 3 x 3 rotation matrices for the aircraft to world [$\mathbf{R}^a_w$], and camera to aircraft [$\mathbf{R}^i_a$] system:

$$\begin{bmatrix} x_w \\ y_w \\ z_w \end{bmatrix} = [\mathbf{R}^a_w][\mathbf{R}^i_a] \begin{bmatrix} x_i \\ y_i \\ z_i \end{bmatrix} \quad . \tag{3}$$

The general form of the two rotation matrices for system 1 to system 2 (either "a" to "w" or "i" to "a") are:

$$[\mathbf{R}^1_2] = \begin{bmatrix} \cos\psi\cos\theta & \cos\psi\sin\theta\sin\phi + \sin\psi\cos\phi & -\cos\psi\sin\theta\cos\phi + \sin\psi\sin\phi \\ -\sin\psi\cos\theta & -\sin\psi\sin\theta\sin\phi + \cos\psi\cos\phi & \sin\psi\sin\theta\cos\phi + \cos\psi\sin\phi \\ \sin\theta & \cos\theta\sin\phi & \cos\theta\cos\phi \end{bmatrix} \tag{4}$$

with $\phi = -(\phi_a - 180°)$, $\theta = \theta_a$, and $\psi = (\psi_a - 90°)$ for aircraft to world coordinates and $\phi = -\phi_i$, $\theta = -\theta_i$, and $\psi = -\psi_i$ for camera to aircraft coordinates.

After coordinate transformation, trigonometric methods are applied to calculate the distance between the camera positions P1 and P2 to the observed point C. Repeating this procedure for a number of points yields a relation between elevation angle and cloud height. For better selection of the tie points, which is done manually the contrast of the images was increased for better identification of recognizable structures of the cloud image. Fig. 6 illustrates the cloud geometry retrieval for a cloud scene from 19 September 2014. The selected cloud case shows a strong convective cloud embedded in a stratiform cloud layer. After

Atmos. Chem. Phys. Discuss., doi:10.5194/acp-2017-64, 2017
Manuscript under review for journal Atmos. Chem. Phys.
Published: 1 February 2017

Atmospheric Chemistry and Physics Discussions

increasing the image contrast (Fig. 6a) several tie points with distinctive cloud features of individual clouds were selected. The same tie points were chosen in a second image taken about 10 seconds later. From stereographic analysis of these tie points the distances to the cloud points were determined (Fig. 6b). From cloud distance and viewing elevation angle the height was calculated. Cloud top heights for this case are in the range of 12 km, while the top of the stratiform layer is at about 6 km altitude. The corresponding isolines in Fig. 6c show quite homogeneous horizontal distribution with negligible dependence on the azimuth angle for this particular cloud case. Therefore, the correlation between elevation angle and height was approximated by a polynomial fit of the third order as plotted in Fig. 6d. This fit was used to relate the elevation angles of the specMACS instrument to a cloud height. For all studied cloud cases of the flights AC10, AC13, and AC18, such simplified correlations between elevation angle and height were determined under the condition that the azimuthal dependence could be neglected which was fulfilled predominantly for sufficiently small cloud sections in the horizontal direction.

The accuracy of the cloud geometry retrieval depends mainly on the distance to the observed cloud and the uncertainty of the angle determination. Uncertainties related to pixel selection were determined with $\pm$ 5 pixels (0.25°), which corresponds to an uncertainty of 130 m for a cloud distance of 30 km (maximum distance of observations). Additionally, the fitting method resulted in mean deviations of 200 m. Overall, uncertainties between 200 and 300 m were calculated for the observing conditions during ACRIDICON-CHUVA.

4 Application

4.1 Case study for flight AC13 (polluted aerosol conditions)

Results of the analysis of one of the 14 scientific flights during ACRIDICON-CHUVA will be presented in this section in more detail. To derive cloud profiles of the phase state based on cloud side spectral reflectivity observations several conditions need to be fulfilled: (i) no cloud layer above the observed cloud (no cirrus), which contaminates the spectral signature, (ii) high proportion of illuminated cloud parts in the vertical direction of the cloud, (iii) flight altitude that allows measurements of an extended vertical region of the cloud considering the limited FOV of specMACS, and (iv) isolated clouds with recognizable structures for cloud geometry retrievals. During flight AC13 on 19 September 2014, several periods of cloud side observations were found that fulfill these conditions. The flight track and the corresponding MODIS image is shown in Fig. 7. The 250 m resolution radiance of channel 1 (620-670 nm) of the MODIS overpass from 17:50 UTC illustrates the cloud coverage. The five colored lines denote the periods of cloud side observations between 17:50 and 19:00 UTC. The white arrows indicate the flight direction with specMACS pointing towards the clouds on the right hand side of the aircraft. The flight altitude for this one-hour flight track ranged between 5 and 10 km. As a result of cloud masking and cloud geometry analysis, the profile of the phase index for a cloud scene (section #A in Fig. 7) is shown in Fig. 8. The phase index is calculated in bins of 100 m in the vertical direction. The standard deviation is indicated by the error bars. A distinctive increase of the phase index is visible at 6.5 km altitude. Below that altitude a negative phase index indicating the liquid water phase was derived. Within the mixed phase layer the phase index increases sharply. The upper limit of the mixed phase layer is derived to be at 7.1 km. Above that altitude the variation of the phase index caused by changing particle sizes and viewing geometry is less pronounced.

Atmos. Chem. Phys. Discuss., doi:10.5194/acp-2017-64, 2017
Manuscript under review for journal Atmos. Chem. Phys.
Published: 1 February 2017

Atmospheric Chemistry and Physics Discussions

Sixteen cloud cases have been investigated for flight AC13. Each cloud scene was classified with respect to the phase state based on the profile of the phase index. Fig. 9a presents the statistics over all scenes. The background color of the scene number corresponds to the flight section as presented in Fig. 7. Obviously not all profiles show each of the three phase states. Mainly because of two reasons. First, the cloud particles may have the same phase state, or, second, the viewing geometry with respect to FOV, flight altitude, cloud height, and distance restricts the vertical range of the cloud observation. Overall, the depth (Δz_{mix}) and vertical position (z_{top}, z_{bottom}) of the mixed phase layer is highly variable for all cases: with Δz_{mix} = 1.2 $\pm$ 0.4 km (one-sigma standard deviation), z_{bottom} = 6.2 $\pm$ 0.3 km, and z_{top} = 7.4 $\pm$ 0.4 km. Even for similar flight sections (as in #B and #D) the upper and lower limit of the mixed phase layer can vary by up to 900 m, which is larger than the uncertainty of the retrieval method. The corresponding temperature scale is displayed as non-linear secondary y-axis.

In situ measurements of CAS-DPOL and hotwire data of the one-hour flight sequence (17:50-19:00 UTC) during AC13 are shown in Fig. 9b,c. The light dots are 1Hz data, while darker lines represent the 10th and 90th percentiles as well as the mean LWC and AF (squares), binned into 600 m altitude bins. Regions of mixed phase clouds are characterized by a decrease in LWC (decrease of the 90th percentile with altitude) and/or an increase in AF. In these in situ measurements of LWC and AF, the mixed phase region extends between 6.4 and 8.7 km. However, the profiles shown in Fig. 9b,c are based on data sampled over the entire cloud cluster including clouds at different stages of evolution, and profiles of individual clouds cannot be derived from this data set, which prevents a direct comparison of the in situ and remote measurements. The asphericity of cloud particles in the size range 20 - 50 μm derived from NIXE-CAPS is shown in Fig. 9d for the one hour time frame of the cloud observations. The data were classified as listed in Tab. 1. The heterogeneity of cloud particle asphericity between 5 and 8 km altitude can be observed from its variable classification during the ascent around 18 UTC with solely spherical particles (could be also related to small spherical ice particles) and during the descent between 18.25 and 18.80 UTC with spherical and aspherical particles. Mainly aspherical particles of Group II were observed, indicating the existence of large ice particles with sizes larger than 50 μm. Except for two single cases, a larger number of spherical particles (open green circles) can be observed up to an altitude of 8 km. From the descent flight track the position of the mixed phase layer is estimated between 6 and 8 km. Exemplarily, a closer look at the asphericity is taken for the time range between 18.28 and 18.34 UTC (Fig. 9e). At a constant flight level near the upper boundary of the mixed phase layer the occurrence of spherical and aspherical particles is somewhat separated. While mainly spherical particles were observed during this selected flight section for vertical wind speeds between $\pm$1 m s$-$1, there are also segments with higher vertical wind speeds (between -3 and 5 m s$-$1). For this section (around 18.315 UTC) large aspherical particles representing ice particles were also measured. This suggests that the vertical distribution of ice and liquid particles is affected by up- and downdrafts within a convective cloud, and therefore it is not homogenous inside the same cloud.

After showing these results from in situ and cloud side measurements, we also present retrievals of the phase state based on cloud top MODIS observations. In Fig. 9f the frequency of liquid and ice phase observations for altitude bins of about 200 m is presented. In these retrievals, no mixed phase was derived for all data in the selected area (Fig. 7). Either fully developed deep convective clouds with cloud tops between 10 and 14 km (classified as ice cloud) or low level cumulus clouds up to 6 km (liquid water clouds) were detected. Cloud phase information from the assumed mixed phase levels are not available, since no

Atmos. Chem. Phys. Discuss., doi:10.5194/acp-2017-64, 2017
Manuscript under review for journal Atmos. Chem. Phys.
Published: 1 February 2017

Atmospheric Chemistry and Physics Discussions

cloud tops with mixed phase were observed. Nevertheless, there are some levels with low frequency classified as ice and liquid phase (8 - 11 km), corresponding to temperatures between -20 and -42°C. In particular, at very low temperatures (lower than -38 °C) the presence of liquid particles can be excluded even for situations of homogeneous freezing. In fact small ice particles may be misinterpreted as liquid particles by the retrieval algorithm at this level (Järvinen et al., 2016).

We applied the ensemble method to derive profiles of the effective particle size and to estimate the glaciation height and temperature following the retrieval technique of Yuan et al. (2010) for the MODIS scene. For better comparison, the brightness temperature as vertical coordinate was converted to altitude. Cloud top brightness temperatures (at 11 μm, corresponding to MODIS Channel 31) were simulated for variable cloud top heights and an atmospheric profile of temperature and humidity as measured by the aircraft. The best agreement of simulated and measured cloud top brightness temperature is used as proxy of the cloud top altitude. The result is presented in Fig. 9g. The particle size is increasing with altitude up to a height of about 9.0 km (horizontal black line). This level is assumed as glaciation height, the upper level of mixed phase layer. The standard deviation of the binned (2 K bins in brightness temperature) particle sizes (horizontal error bars) is significantly larger for altitudes below 11 km, indicating a larger variability of the cloud particle size and a smaller statistics.

Comparing the glaciation height from MODIS with NIXE-CAPS in situ data and results from specMACS observations shows a deviation of about 1.0 - 1.5 km between the different retrieval techniques and observation strategies. However, the mean profile over the entire cloud cluster derived from CAS-DPOL measurements exhibited a similar glaciation height (of about 8.7 km) as found from the MODIS data. This shows that the satellite-based ensemble method may be representative for a large cloud field, but that for individual clouds, particularly in their later stage of evolution, the particle phase may be altered by up- and downdrafts as observed by the NIXE-CAPS and specMACS measurements.

4.2 Comparison with less polluted conditions

Profiles of the phase state for two other flights (AC10 and AC18) performed under moderate aerosol conditions are presented in Fig.10. On both days the number of complete profiles showing all three phases is limited compared to AC13. Mainly low level clouds or cloud parts with liquid water were observed on AC18. The lower boundary of the mixed phase layer is estimated to be about 5.5 km (-4°C). From NIXE-CAPS measurements, large aspherical ice particles were measured down to 5 km (-1°C), whereas spherical particles assumed to be as liquid water were found up to 8.7 km (not shown). In contrast, the specMACS data exhibit ice phase down to 7.7 km. As in the case of AC13, the cloud top MODIS retrievals of the phase state only distinguished between liquid and ice phase. Because of the low statistical significance of clouds with cloud tops higher than 6 km in the MODIS data, no profile of effective drop radius was derived. From theory the mixed phase layer is expected to be higher for polluted aerosol conditions than for cleaner aerosol conditions, which could not be confirmed by the studied cases. It was evident, however, that the lower boundary altitude of the mixed phase layer tends to be higher for polluted conditions (AC13: 6.0 - 6.5 km) than for the moderate case of AC18. On flight AC10 no in situ data within mixed phase clouds was obtained. Also the MODIS phase product shows either ice (cloud tops between 11 and 15 km altitude) or liquid water (clouds up to 4.5 km). But the profile of the effective particle radius based on the ensemble method retrieval gives a glaciation temperature of 260 K, which corresponds to an altitude of about 7.2 km. The specMACS profiles as plotted in Fig. 10b show highly variable

Atmos. Chem. Phys. Discuss., doi:10.5194/acp-2017-64, 2017
Manuscript under review for journal Atmos. Chem. Phys.
Published: 1 February 2017

Atmospheric Chemistry and Physics Discussions

mixed phase layers. While clouds #1 - #3 with cloud tops between 6.0 - 6.8 km were classified as liquid water clouds, the profile of the phase index of clouds #4 - #6 reveal also the existence of ice particles between 4 and 7 km altitude. As illustrated in the RGB image taken by the GoPro camera (Fig. 10c), cloud #3 and #4 were in close vicinity but in different states of evolution. The diffuse looking cloud areas with smoother texture in the GoPro image of cloud #4 indicate precipitation, which explains positive phase indices down to 4 km corresponding to 0°C. As Fig. 10d clearly shows, the phase index can vary significantly for one altitude level depending on the occurrence of precipitation. Consequently, the individual state of evolution of each cloud determines the distribution of particle sizes and phase state. Also strong downdrafts can transport ice particles into lower levels, which will be interpreted as mixed phase layer from the cloud side observation perspective, whereas in situ measurements inside the cloud only reveal liquid phase particles.

5 Conclusions

The vertical evolution of deep convective clouds is linked with the phase transition from liquid water to mixed phase and to the ice phase. Aerosol particles may alter the radiative effects of cloud particles (also with respect to their phase state), their lifetime and the formation of precipitation. This study documents the vertical distribution of the three phase states for different aerosol conditions as measured during the ACRIDICON-CHUVA campaign over the Brazilian Amazon in September 2014. A different approach than the traditional in situ and satellite observations was presented, which is mainly focused on the retrieval of the mixed phase layer. Cloud side observations performed by the imaging spectroradiometer specMACS were used to determine a phase index based on differential absorption by ice and liquid water in the spectral range between 1550 and 1700 nm. Negative values of the phase index indicate liquid particles, whereas ice particles cause a positive phase index. It was additionally shown by 3D radiative transfer simulations that the mixed phase zone is characterized by a distinctive change of gradient in the profile of the phase index. A cloud mask method to discriminate between shadowed and illuminated cloud regions was presented to exclude the shadowed areas in the cloud scene due to their contaminated spectral information. We also performed 3D radiative transfer simulations for a complex cloud field to validate the approach of using histograms of RGB color values for the discrimination method. Since specMACS delivers spectral radiation data as a function of viewing zenith angle, the derived mean vertical profiles of the phase index needed to be referenced to altitude ranges. For this purpose, stereographic methods were applied to collocated GoPro camera observations to estimate the cloud geometry in terms of cloud height profiles and distance to the aircraft.

The profiles of several individual clouds were classified with respect to their zones of phase states. Depending on the viewing geometry and cloud distance, all three phases were found for deep convective clouds. In particular the layer of phase transition was highly variable (900 m in upper and lower limit) in its height and vertical thickness even for one compact cloud cluster measured during flight AC13 with polluted aerosol conditions. Here first ice particles were found at temperatures between -3 and -9 °C, while full glaciation was observed between -10 and -20 °C. Only few cases showing all three phase states were observed for moderate aerosol conditions. Because of the low statistics, a decrease of glaciation temperature for polluted aerosol conditions compared to the moderate case of flight AC18 could not be observed. However, the occurrence of first ice particles was found for polluted conditions between 6.0 - 6.5 km, whereas for AC18 the altitude was shifted down to 5.5 - 6.0 km, which agrees with theory.

Also, in situ measurements of the cloud particle size distribution together with the asphericity of particles between 20 and 50 μm, measured by the cloud spectrometer NIXE-CAPS, were used to estimate the cloud's phase (Costa et al., 2017). Aspherical hydrometeor particles can be considered as ice, whereas spherical shapes are related to liquid droplets or spherical ice. In contrast to cloud-side remote sensing by specMACS, in situ observations represent point measurements within the cloud. Therefore, in situ profile information of an individual cloud is a combination of data from different time steps and therefore states of evolution. Despite the different observation perspectives, consistent results were found with similar mixed phase zone levels.

Aerosol effects on the glaciation temperature in deep convective clouds were studied with an ensemble method using MODIS data, which assumes the invariance of space and time for a cluster of clouds with different states of evolution. For the polluted and moderate flights, retrieval results of the effective particle size at cloud top were combined into one single profile. For flight AC13 the glaciation height of 9.0 km (-26°C), defined by the level of maximum particle size, deviates from the in situ (8 km) and specMACS results (6.8 - 8.2 km). However, for the moderate aerosol case the glaciation height is much lower at about 7.2 km (-13°C), similar to the height derived from specMACS observations (7 km).

The presented study shows that the occurrence of ice particles and the level of the mixed phase layer vary by several hundred of meters even for similar atmospheric conditions. Two cloud cases in close vicinity clearly show different cloud phases at the same altitude. It is assumed that downdrafts and falling precipitation in well-developed clouds alter the retrieval results of the phases' vertical distribution. Finally, we can conclude that the assumed space-time-invariance used in the ensemble method can give only a simplified picture of the vertical distribution of the phase within a field of convective clouds of different stages of evolution.

Planned future studies include observations of individual convective clouds to document their evolution from growing to mature and finally to dissipating stages of development. We intend to deploy our sensor on ATTO (Andreae et al., 2015), which is 325 m high and is used to perform continuous monitoring of chemical, meteorological and aerosol parameters. The ATTO tower is located near the Equator (a region with daily occurrence of DCCs in a highly variable environment with respect to concentrations and types of aerosol particles) and will serve as an ideal platform for upcoming studies.

Acknowledgements. The ACRIDICON-CHUVA campaign was supported by the Max Planck Society (MPG), the German Science Foundation (DFG Priority Program SPP 1294), the German Aerospace Center (DLR), the FAPESP (Sao Paulo Research Foundation) grants 2009/15235-8 and 2013/05014-0), and a wide range of other institutional partners. It was carried out in collaboration with the USA–Brazilian atmosphere research project GoAmazon2014/5, including numerous institutional partners. We would like to thank Instituto Nacional de Pesquisas da Amazonia (INPA) for the local logistic help prior, during, and after the campaign. Thanks also to the Brazilian Space Agency (AEB: Agencia Espacial Brasileira) responsible for the program of cooperation (CNPq license 00254/2013-9 of the Brazilian National Council for Scientific and Technological Development). The entire ACRIDICON-CHUVA project team is gratefully acknowledged for collaboration and support. Evelyn Jäkel gratefully acknowledges funding of parts of this work by the German Research Foundation (DFG) under grant number (JA2023/2-2).

Atmos. Chem. Phys. Discuss., doi:10.5194/acp-2017-64, 2017
Manuscript under review for journal Atmos. Chem. Phys.
Published: 1 February 2017

Atmospheric Chemistry and Physics Discussions

References

Albrecht, B. A.: Aerosols, Cloud Microphysics, and Fractional Cloudiness, Science, 245, 1227–1230, http://www.sciencemag.org/content/245/4923/1227.abstract, 1989.

Anderson, G., Clough, S., Kneizys, F., Chetwynd, J., and Shettle, E.: AFGL Atmospheric Constituent Profiles (0–120 km), Tech. Rep. AFGL-TR-86-0110, AFGL (OPI), Hanscom AFB, MA 01736, 1986.

Andreae, M. O., Rosenfeld, D., Artaxo, P., Costa, A. A., Frank, G. P., Longo, K. M., and Silva-Dias, M. A. F.: Smoking rain clouds over the Amazon, Science, 303, 1337–1342, doi:10.1126/science.1092779, 2004.

Andreae, M. O., Acevedo, O. C., Araùjo, A., Artaxo, P., Barbosa, C. G. G., Barbosa, H. M. J., Brito, J., Carbone, S., Chi, X., Cintra, B. B. L., da Silva, N. F., Dias, N. L., Dias-Júnior, C. Q., Ditas, F., Ditz, R., Godoi, A. F. L., Godoi, R. H. M., Heimann, M., Hoffmann, T., Kesselmeier, J., Könemann, T., Krüger, M. L., Lavric, J. V., Manzi, A. O., Lopes, A. P., Martins, D. L., Mikhailov, E. F., Moran-Zuloaga, D., Nelson, B. W., Nölscher, A. C., Santos Nogueira, D., Piedade, M. T. F., Pöhlker, C., Pöschl, U., Quesada, C. A., Rizzo, L. V., Ro, C.-U., Ruckteschler, N., Sá, L. D. A., de Oliveira Sá, M., Sales, C. B., dos Santos, R. M. N., Saturno, J., Schöngart, J., Sörgel, M., de Souza, C. M., de Souza, R. A. F., Su, H., Targhetta, N., Tóta, J., Trebs, I., Trumbore, S., van Eijck, A., Walter, D., Wang, Z., Weber, B., Williams, J., Winderlich, J., Wittmann, F., Wolff, S., and Yáñez Serrano, A. M.: The Amazon Tall Tower Observatory (ATTO): overview of pilot measurements on ecosystem ecology, meteorology, trace gases, and aerosols, Atmos. Chem. Phys., 15, 10 723–10 776, doi:10.5194/acp-15-10723-2015, http://www.atmos-chem-phys.net/15/10723/2015/, 2015.

Baum, B. A., Heymsfield, A. J., Yang, P., and Bedka, S. T.: Bulk scattering properties for the remote sensing of ice clouds. Part I: Microphysical data and models, J. Appl. Meteor., 44, 1885–1895, 2005.

Baum, B. A., Yang, P., Nasiri, S., Heidinger, A. K., Heymsfield, A., and Li, J.: Bulk scattering properties for the remote sensing of ice clouds. Part III: High-resolution spectral models from 100 to 3250 cm^{-1}, J. Appl. Meteor., 46, 423–434, 2007.

Bodhaine, B., Wood, N., Dutton, E., and Slusser, J.: On Rayleigh oprical depth calculations, J. Atmos. Oceanic Technol., 16, 1854–1861, 1999.

Bradski, G. and Kaehler, A.: Learning OpenCV: Computer Vision in C++ with the OpenCV Library, O'Reilly Media, Inc., 2nd edn., 2013.

Braga, R. C., Rosenfeld, D., Weigel, R., Jurkat, T., Andreae, M. O., Wendisch, M., Pöhlker, M. L., Klimach, T., Pöschl, U., Pöhlker, C., Voigt, C., Mahnke, C., Borrmann, S., Albrecht, R. I., Molleker, S., Vila, D. A., Machado, L. A. T., and Artaxo, P.: Comparing calculated microphysical properties of tropical convective clouds at cloud base with measurements during the ACRIDICON-CHUVA campaign, Atmospheric Chemistry and Physics Discussions, 2016, 1–46, doi:10.5194/acp-2016-872, http://www.atmos-chem-phys-discuss.net/acp-2016-872/, 2016.

Cahalan, R.: Bounded cascade clouds: albedo and effective thickness, Nonlin. Proc. Geophys., 1, 1994.

Cecchini, M. A., Machado, L. A. T., Andreae, M. O., Martin, S. T., Albrecht, R. I., Artaxo, P., Barbosa, H. M. J., Borrmann, S., Fütterer, D., Jurkat, T., Mahnke, C., Minikin, A., Molleker, S., Pöhlker, M. L., Pöschl, U., Rosenfeld, D., Voigt, C., Weinzierl, B., and Wendisch, M.: Amazonian clouds are more sensitive to changes in pollution than in thermodynamic conditions, to be submitted to J. Geophys. Res., 2017.

Costa, A., Meyer, J., Afchine, A., Luebke, A., Dorsey, J. R., Gallagher, M. W., Ehrlich, A., Wendisch, M., Baumgardner, D., and Krämer, M.: Classification of Arctic, Mid-Latitude and Tropical Clouds in the Mixed-Phase Temperature Regime, to be submitted to ACP, 2017.

Ehrlich, A., Bierwirth, E., Wendisch, M., Gayet, J.-F., Mioche, G., Lampert, A., and Heintzenberg, J.: Cloud phase identification of Arctic boundary-layer clouds from airborne spectral reflection measurements: Test of three approaches, Atmos. Chem. Phys., 8, 7493–7505, 2008.

Ewald, F., Winkler, C., and Zinner, T.: Reconstruction of cloud geometry using a scanning cloud radar, Atmos. Meas. Tech., 8, 2491–2508, doi:10.5194/amt-8-2491-2015, 2015.

Ewald, F., Kölling, T., Baumgartner, A., Zinner, T., and Mayer, B.: Design and characterization of specMACS, a multipurpose hyperspectral cloud and sky imager, Atmos. Meas. Technol., 9, 2015–2042, doi:doi:10.5194/amt-9-2015-2016, 2016.

Freud, E., Rosenfeld, D., Andreae, M. O., Costa, A. A., and Artaxo, P.: Robust relations between CCN and the vertical evolution of cloud drop size distribution in deep convective clouds, Atmos. Chem. Phys., 8, 1661–1675, 2008.

Hartley, R. I. and Zisserman, A.: Multiple View Geometry in Computer Vision, Cambridge University Press, ISBN: 0521540518, second edn., 2004.

Hu, J., Razdan, A., and Zehnder, J. A.: Geometric Calibration of Digital Cameras for 3D Cumulus Cloud Measurements, J. Atmos. Oceanic Technol., 26, 200–214, doi:10.1175/2008JTECHA1079.1, http://dx.doi.org/10.1175/2008JTECHA1079.1, 2009.

Iwabuchi, H.: Efficient Monte Carlo methods for radiative transfer modeling, J. Atmos. Sci., 63, 2324–2339, 2006.

Jäkel, E., Walther, J., and Wendisch, M.: Thermodynamic phase retrieval of convective clouds: impact of sensor viewing geometry and vertical distribution of cloud properties, Atmos. Meas. Tech., 6, 539–547, doi:10.5194/amt-6-539-2013, 2013.

Jäkel, E., Wendisch, M., Ewald, F., and Kölling, T.: Analysis of the Vertical Distribution of the Thermodynamic Phase in Tropical Deep-convective Clouds, in: Light, Energy and the Environment, p. HTu2F.1, Optical Society of America, doi:10.1364/HISE.2016.HTu2F.1, http://www.osapublishing.org/abstract.cfm?URI=HISE-2016-HTu2F.1, 2016.

Järvinen, E., Schnaiter, M., Mioche, G., Jourdan, O., Shcherbakov, V. N., Costa, A., Afchine, A., Krämer, M., Heidelberg, F., Jurkat, T., Voigt, C., Schlager, H., Nichman, L., Gallagher, M., Hirst, E., Schmitt, C., Bansemer, A., Heymsfield, A., Lawson, P., Tricoli, U., Pfeilsticker, K., Vochezer, P., Möhler, O., and Leisner, T.: Quasi-Spherical Ice in Convective Clouds, Journal of the Atmospheric Sciences, 73, 3885–3910, doi:10.1175/JAS-D-15-0365.1, http://dx.doi.org/10.1175/JAS-D-15-0365.1, 2016.

Khain, A., Prabha, T. V., Benmoshe, N., Pandithurai, G., and Ovchinnikov, M.: The mechanism of first raindrops formation in deep convective clouds, Journal of Geophysical Research: Atmospheres, 118, 9123–9140, doi:10.1002/jgrd.50641, http://dx.doi.org/10.1002/jgrd.50641, 2013.

Konwar, M., Maheskumar, R. S., Kulkarni, J. R., Freud, E., Goswami, B. N., and Rosenfeld, D.: Aerosol control on depth of warm rain in convective clouds, Journal of Geophysical Research: Atmospheres, 117, n/a–n/a, doi:10.1029/2012JD017585, http://dx.doi.org/10.1029/2012JD017585, d13204, 2012.

Luebke, A. E., Afchine, A., Costa, A., Grooß, J.-U., Meyer, J., Rolf, C., Spelten, N., Avallone, L. M., Baumgardner, D., and Krämer, M.: The origin of midlatitude ice clouds and the resulting influence on their microphysical properties, Atmospheric Chemistry and Physics, 16, 5793–5809, doi:10.5194/acp-16-5793-2016, http://www.atmos-chem-phys.net/16/5793/2016/, 2016.

Martins, J. V., Marshak, A., Remer, L. A., Rosenfeld, D., Kaufman, Y. J., Fernandez-Borda, R., Koren, I., Correia, A. L., Zubko, V., and Artaxo, P.: Remote sensing the vertical profile of cloud droplet effective radius, thermodynamic phase, and temperature, Atmos. Chem. Phys., 11, 9485–9501, doi:10.5194/acp-11-9485-2011, 2011.

Meyer, J.: Ice Crystal Measurements with the New Particle Spectrometer NIXE-CAPS, Dr. (univ.), Jülich, http://juser.fz-juelich.de/record/22871, record converted from VDB: 12.11.2012; Wuppertal,Univ., Diss., 2012, 2012.

Nicolet, M., Stetzer, O., and Lohmann, U.: Depolarization ratios of single ice particles assuming finite circular cylinders, Appl. Opt., 46, 4465–4476, doi:10.1364/AO.46.004465, http://ao.osa.org/abstract.cfm?URI=ao-46-20-4465, 2007.

Pierluissi, J. and Peng, G.-S.: New molecular transmission band models for LOWTRAN, Opt. Eng., 24, 541–547, 1985.

Pilewskie, P. and Twomey, S.: Discrimination of ice from water in clouds by optical remote sensing, Atmos. Res., 21, 113–122, 1987.

Platnick, S., King, M., Ackerman, S., Menzel, W., Baum, B., Riedi, J., and Frey, R.: The MODIS cloud products: Algorithms and examples from TERRA, IEEE Trans. Geosci. Remote Sens., 41, 459–473, 2003.

Ricchiazzi, P. and Gautier, C.: Investigation of the effect of surface heterogeneity and topography on the radiation environment of Palmer Station, Antarctica, with a hybrid 3-D radiative transfer model, J. Geophys. Res., 103, 6161–6178, 1998.

Rosenfeld, D. and Feingold, G.: Explanations of discrepancies among satellite observations of the aerosol indirect effects, Geophys. Res. Lett., 30, doi:10.1029/2003GL017 684, 2003.

Rosenfeld, D. and Lensky, I. M.: Satellite-based insights into precipitation formation processes in continental and maritime convective clouds, Bull. Amer. Meteor. Soc., 79, 2457–2476, 1998.

Rosenfeld, D. and Woodley, W. L.: Deep convective clouds with sustained supercooled liquid water down to-37.5 C, Nature, 405, 440–442, 2000.

Rosenfeld, D. and Woodley, W. L.: Spaceborne Inferences of Cloud Microstructure and Precipitation Processes: Synthesis, Insights, and Implications, Meteorological Monographs, 51, 59–80, doi:10.1175/0065-9401(2003)029<0059:CSIOCM>2.0.CO;2, http://dx.doi.org/10.1175/0065-9401(2003)029<0059:CSIOCM>2.0.CO;2, 2003.

Rosenfeld, D., Lohmann, U., Raga, G. B., O'Dowd, C. D., Kulmala, M., Fuzzi, S., Reissell, A., and Andreae, M. O.: Flood or drought: How do aerosols affect precipitation?, Science, 321, 1309–1313, 2008.

Rosenfeld, D., Liu, G., Yu, X., Zhu, Y., Dai, J., Xu, X., and Yue, Z.: High-resolution (375 m) cloud microstructure as seen from the NPP/VIIRS satellite imager, Atmos. Chem. Phys., 14, 2479–2496, doi:10.5194/acp-14-2479-2014, http://www.atmos-chem-phys.net/14/2479/2014/, 2014.

Schnaiter, M., Järvinen, E., Vochezer, P., Abdelmonem, A., Wagner, R., Jourdan, O., Mioche, G., Shcherbakov, V. N., Schmitt, C. G., Tricoli, U., Ulanowski, Z., and Heymsfield, A. J.: Cloud chamber experiments on the origin of ice crystal complexity in cirrus clouds, Atmospheric Chemistry and Physics, 16, 5091–5110, doi:10.5194/acp-16-5091-2016, http://www.atmos-chem-phys.net/16/5091/2016/, 2016.

Schwarzmaier, T., Baumgartner, A., Gege, P., Köhler, C., and Lenhard, K.: DLR's New Traceable Radiance Standard "RASTA", in: International Geoscience and Remote sensing Symposium (IEEE, 2012), pp. 1–4, 2012.

Seiz, G. and Davies, R.: Reconstruction of cloud geometry from multi-view satellite images, REMOTE SENSING OF ENVIRONMENT, 100, 143–149, doi:10.1016/j.rse.2005.09.016, 2006.

Shettle, E.: Comments on the use of LOWTRAN in transmission calculations for sites with the ground elevated relative to sea level, Appl. Opt., 28, 1451–1452, 1989.

Tao, W.-K., Starr, D., Hou, A., Newman, P., and Sud, Y.: A cumulus parmeterization workshop, Bull. Amer. Meteorol. Soc., 84, 1055–1062, 2003.

Tao, W.-K., Chen, J.-P., Li, Z., Wang, C., and Zhang, C.: Impact of aerosols on convective clouds and precipitation, Reviews of Geophysics, 50, 1–62, doi:10.1029/2011RG000369, http://dx.doi.org/10.1029/2011RG000369, rG2001, 2012.

Twomey, S.: The influence of pollution on the shortwave albedo of clouds, J. Atmos. Sci., 34, 1149–1152, 1977.

Voigt, C., Schumann, U., Minikin, A., Abdelmonem, A., Afchine, A., Borrmann, S., Boettcher, M., Buchholz, B., Bugliaro, L., Costa, A., Curtius, J., Dollner, M., Dörnbrack, A., Dreiling, V., Ebert, V., Ehrlich, A., Fix, A., Forster, L., Frank, F., Fütterer, D., Giez, A., Graf,

K., Grooß, J.-U., Groß, S., Heimerl, K., Heinold, B., Hüneke, T., Järvinen, E., Jurkat, T., Kaufmann, S., Kenntner, M., Klingebiel, M., Klimach, T., Kohl, R., Krämer, M., Krisna, T. C., Luebke, A., Mayer, B., Mertes, S., Molleker, S., Petzold, A., Pfeilsticker, K., Port, M., Rapp, M., Reutter, P., Rolf, C., Rose, D., Sauer, D., Schäfler, A., Schlage, R., Schnaiter, M., Schneider, J., Spelten, N., Spichtinger, P., Stock, P., Walser, A., Weigel, R., Weinzierl, B., Wendisch, M., Werner, F., Wernli, H., Wirth, M., Zahn, A., Ziereis, H., and Zöger, M.: ML-CIRRUS - The airborne experiment on natural cirrus and contrail cirrus with the high-altitude long-range research aircraft HALO, Bulletin of the American Meteorological Society, doi:10.1175/BAMS-D-15-00213.1, http://dx.doi.org/10.1175/BAMS-D-15-00213.1, 2016.

Wendisch, M., Pöschl, U., Andreae, M. O., Machado, L. A. T., Albrecht, R., Schlager, H., Rosenfeld, D., Martin, S. T., Abdelmonem, A., Afchine, A., Araujo, A., Artaxo, R., Aufmhoff, H., Barbosa, H. M. J., Borrmann, S., Braga, R., Buchholz, B., Cecchini, M. A., Costa, A., Curtius, J., Dollner, M., Dorf, M., Dreiling, V., Ebert, V., Ehrlich, A., Ewald, F., Fisch, G., Fix, A., Frank, F., Fütterer, D., Heckl, C., Heidelberg, F., Hüneke, T., Jäkel, E., Järvinen, E., Jurkat, T., Kanter, S., Kästner, U., Kenntner, M., Kesselmeier, J., Klimach, T., Knecht, M., Kohl, R., Kölling, T., Krämer, M., Krüger, M., Krisna, T. C., Lavric, J. V., Longo, K., Mahnke, C., Manzi, A. O., Mayer, B., Mertes, S., Minikin, A., Molleker, S., Münch, S., Nillius, B., Pfeilsticker, K., Pöhlker, C., Roiger, A. E., Rose, D., Rosenow, D., Sauer, D., Schnaiter, M., Schneider, J., Schulz, C., de Souza, R. A. F., Spanu, A., Stock, P., Vila, D., Voigt, C., Walser, A., Walter, D., Weigel, R., Weinzierl, B., Werner, R., Yamasoe, M. A., Ziereis, H., Zinner, T., and Zöger, M.: The ACRIDICON-CHUVA campaign: Studying tropical deep convective clouds and precipitation over Amazonia using the new German research aircraft HALO, Bull. Am. Meteorol. Soc., doi:10.1175/BAMS-D-14-00255.1, 2016.

Yuan, T., Martins, J. V., Li, Z., and Remer, L. A.: Estimating glaciation temperature of deep convective clouds with remote sensing data, Geophys. Res. Lett., 37, doi:10.1029/2010GL042753, 2010.

Zinner, T., Marshak, A., Lang, S., Martins, J. V., and Mayer, B.: Remote sensing of cloud sides of deep convection: towards a three-dimensional retrieval of cloud particle size profiles, Atmos. Chem. Phys., 8, 4741–4757, 2008.

Atmos. Chem. Phys. Discuss., doi:10.5194/acp-2017-64, 2017
Manuscript under review for journal Atmos. Chem. Phys.
Published: 1 February 2017

Atmospheric Chemistry and Physics Discussions

Table 1. Cloud flag description of the NIXE-CAPS asphericity product after Costa et al. (2017). Group I: total concentration of particles 3-50 μm is larger than 3 cm^{-3}, Group II: total concentration of particles 3-50 μm is smaller than 1 cm^{-3} and total concentration of particles with size larger than 50 μm is larger than 0 cm^{-3}.

Cloud flag	Temperature range (°C)	Description
1.0	> 0	no aspherical particles detected; liquid
1.1	> 0	aspherical particles detected - could be ice or ash particles
2.0	$0 > T >$ -38	no aspherical particles detected; liquid
2.1	$0 > T >$ -38	aspherical particles detected, group I; mixed phase
2.2	$0 > T >$ -38	aspherical particles detected, group II; ice
3.0	< -38	below homogeneous freezing threshold: all ice, no asphericity criterion; ice

Atmos. Chem. Phys. Discuss., doi:10.5194/acp-2017-64, 2017
Manuscript under review for journal Atmos. Chem. Phys.
Published: 1 February 2017

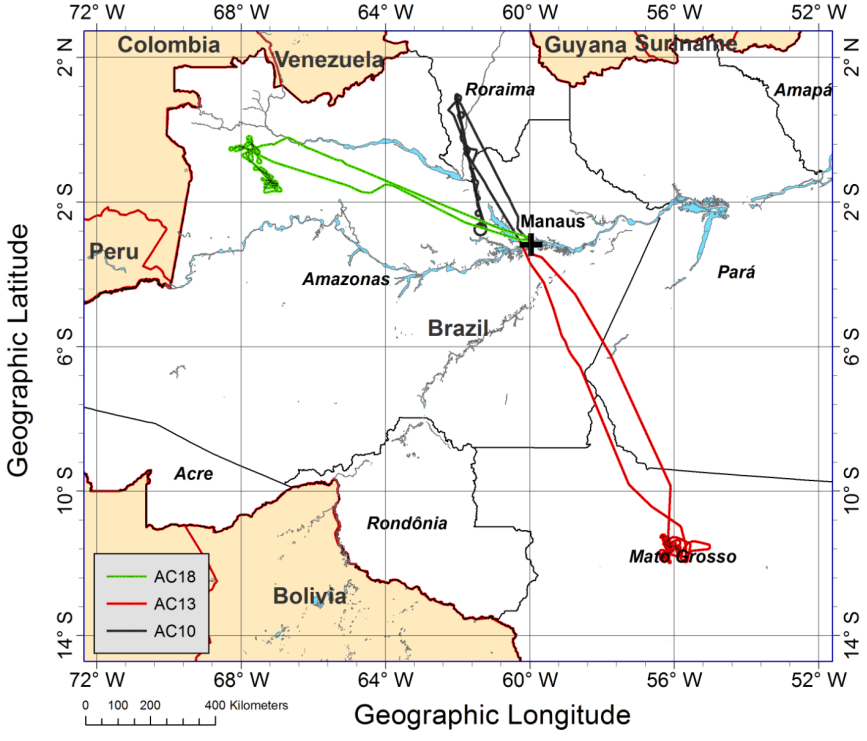

Figure 1. Flight tracks of AC10 (black), AC13 (red), and AC18 (green). The city of Manaus is indicated by the black cross.

Atmos. Chem. Phys. Discuss., doi:10.5194/acp-2017-64, 2017
Manuscript under review for journal Atmos. Chem. Phys.
Published: 1 February 2017

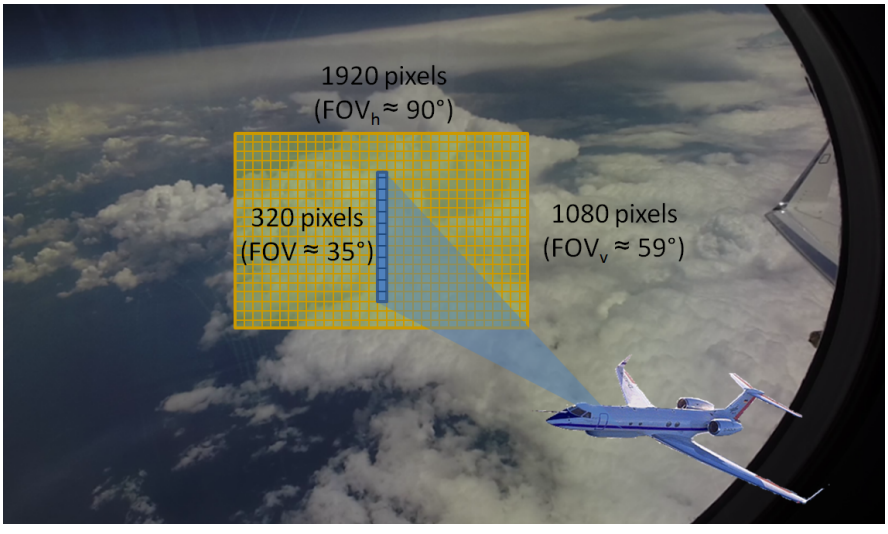

Figure 2. Schematics of cloud side observations by the imaging spectrometer specMACS (SWIR camera) and the GoPro camera. The individual field of views (FOVs) and corresponding number of spatial pixels are illustrated.

Atmos. Chem. Phys. Discuss., doi:10.5194/acp-2017-64, 2017
Manuscript under review for journal Atmos. Chem. Phys.
Published: 1 February 2017

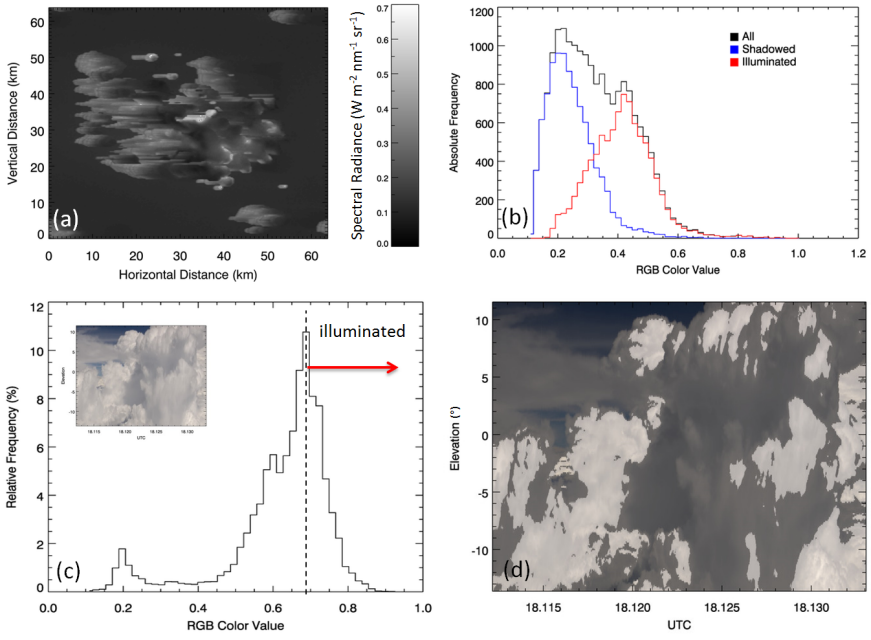

Figure 3. (a) Field of RGB color values from simulated spectral radiances for cloud side viewing geometry with a sensor elevation angle of 10° and a relative azimuth angle of 60°. (b) Histograms of RGB color values of the field shown in (a). (c) Histogram of RGB color values for a measured cloud scene shown in the insert. (d) Identified illuminated cloud sides of the observed cloud scene are highlighted in brighter colors.

Atmos. Chem. Phys. Discuss., doi:10.5194/acp-2017-64, 2017
Manuscript under review for journal Atmos. Chem. Phys.
Published: 1 February 2017

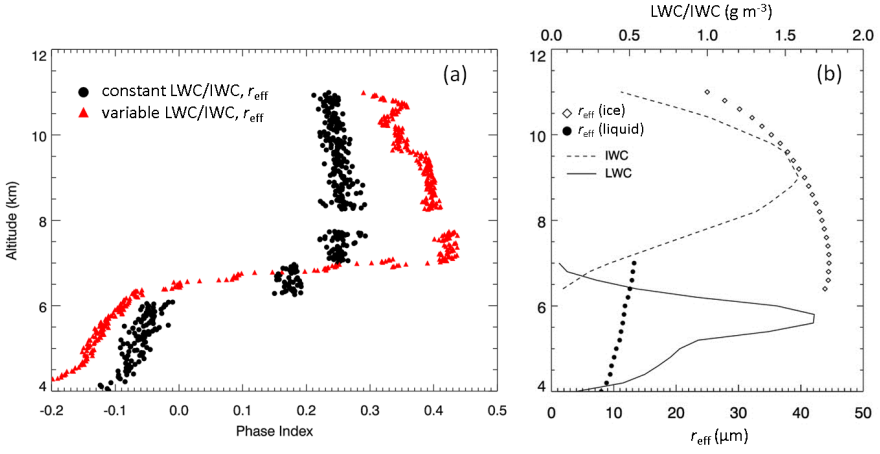

Figure 4. (a) Phase index derived for simulated clouds with variable LWC/IWC and effective radius and fixed values of microphysical properties. (b) Profile of corresponding cloud with variable LWC/IWC and r_{eff}.

Atmos. Chem. Phys. Discuss., doi:10.5194/acp-2017-64, 2017
Manuscript under review for journal Atmos. Chem. Phys.
Published: 1 February 2017

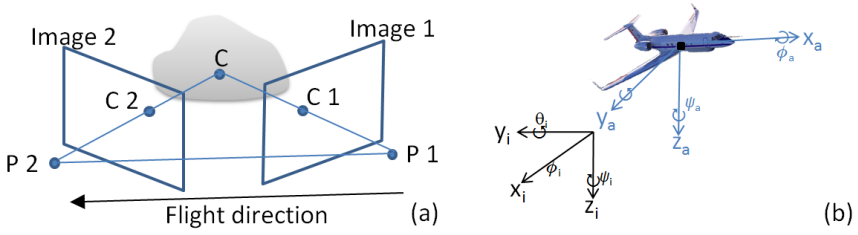

Figure 5. (a) Schematics of stereo-photogrammetric observations of cloud point C from aircraft position P1 and P2 with projected image points C1 and C2. (b) Illustration of aircraft and camera coordinate systems.

Atmos. Chem. Phys. Discuss., doi:10.5194/acp-2017-64, 2017
Manuscript under review for journal Atmos. Chem. Phys.
Published: 1 February 2017

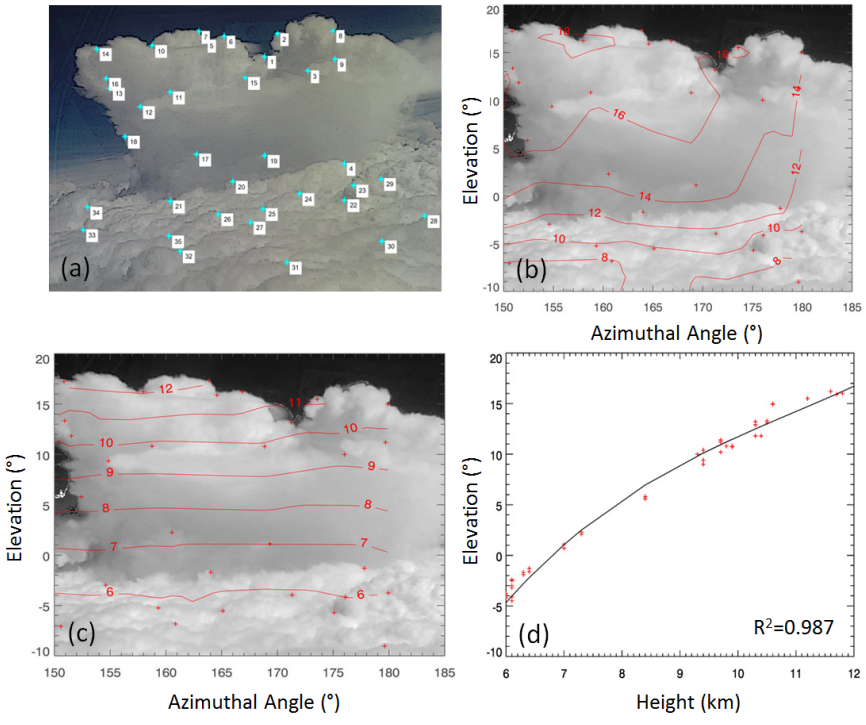

Figure 6. (a) Cloud image from GoPro camera with enhanced edges and selected tie points from 19 September 2014. (b) Calculated distances in km to the individual cloud points for the cloud scene displayed as isolines. (c) Corresponding isolines of calculated heights. (d) Relationship of height and elevation angle derived for the cloud case including a polynomial fit with a correlation coefficient of $R^2 = 0.987$.

Atmos. Chem. Phys. Discuss., doi:10.5194/acp-2017-64, 2017
Manuscript under review for journal Atmos. Chem. Phys.
Published: 1 February 2017

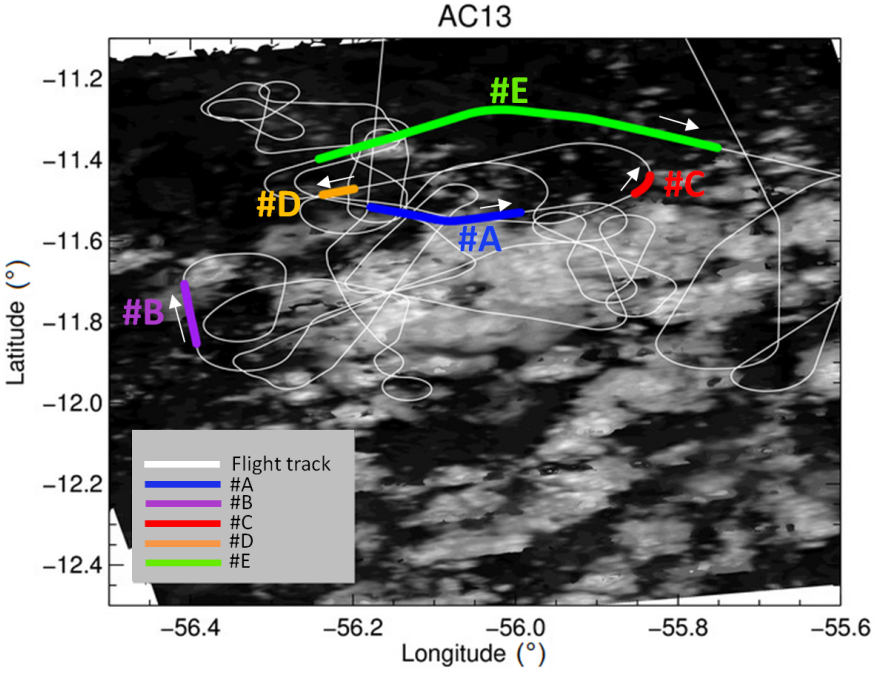

Figure 7. Flight track (white line) and selected time periods of cloud side observations during AC13 (19 September 2014). Additionally, the 250 m resolution product for channel 1 (620 - 670 nm) of the Aqua-MODIS instrument from 17:50 UTC is shown in the background. Figure is similar as presented in Jäkel et al. (2016).

Atmos. Chem. Phys. Discuss., doi:10.5194/acp-2017-64, 2017
Manuscript under review for journal Atmos. Chem. Phys.
Published: 1 February 2017

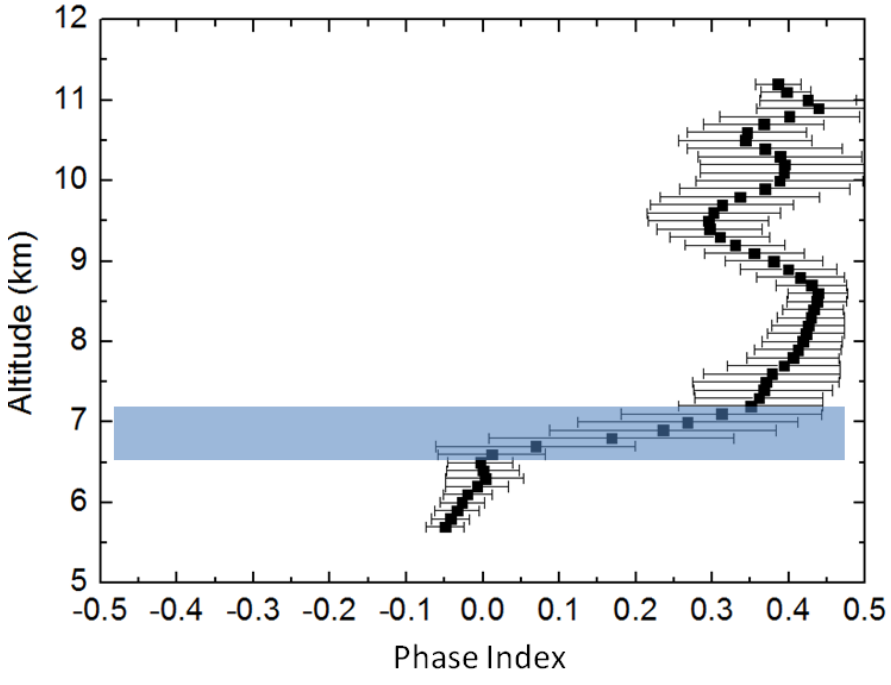

Figure 8. Mean phase index profile for cloud scene shown in Fig. 6. The mixed phase layer is indicated by the colored area.

Atmos. Chem. Phys. Discuss., doi:10.5194/acp-2017-64, 2017
Manuscript under review for journal Atmos. Chem. Phys.
Published: 1 February 2017

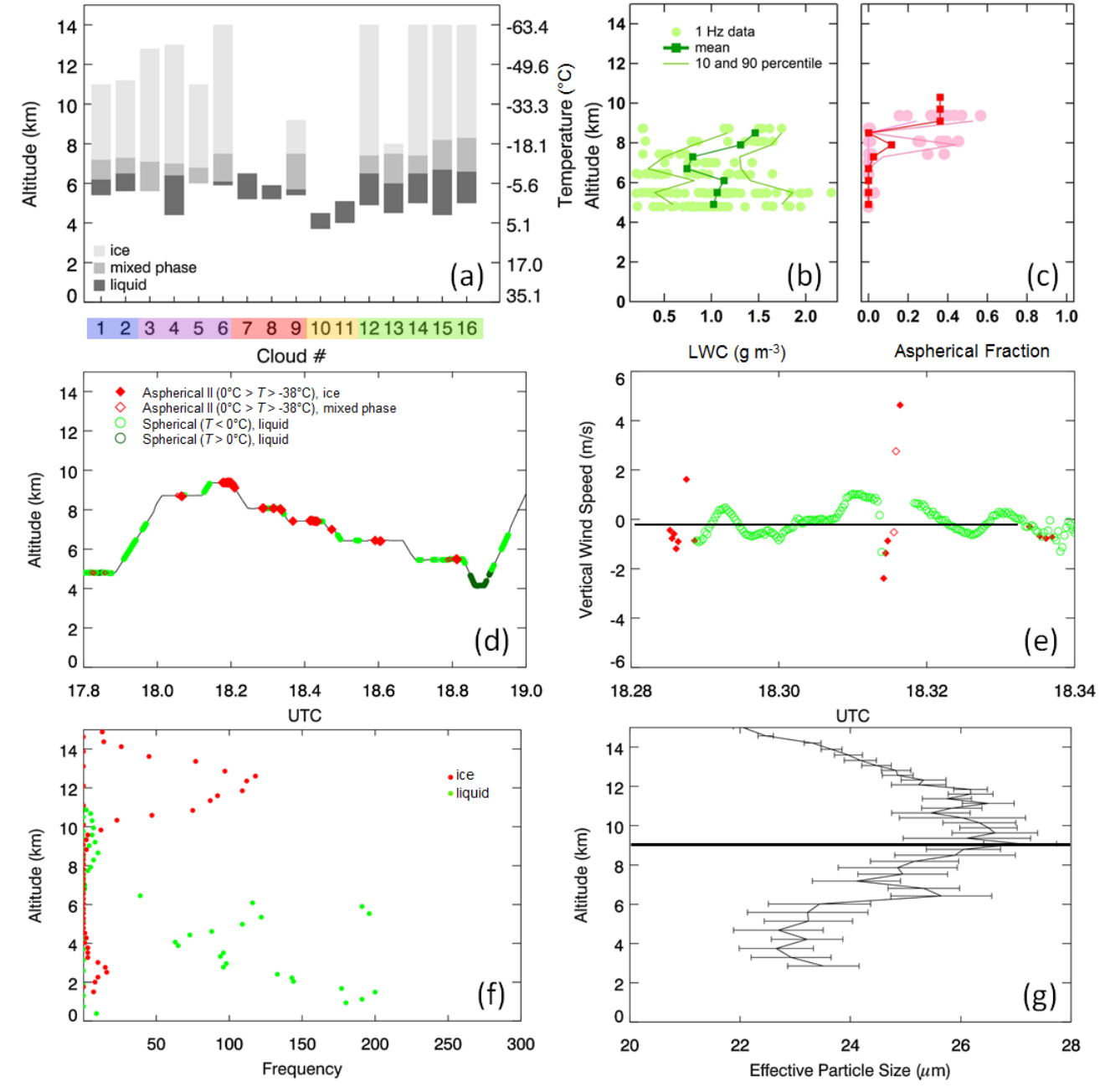

Figure 9. (a) Phase classification of studied clouds based on specMACS observations during flight AC13. (b) Profile of LWC measured with the hotwire probe between 17:50 and 19:00 UTC. (c) Aspherical fraction derived from CAS-DPOL in situ data. (d) NIXE-CAPS in situ measurements of liquid, mixed phase and ice, see Table 1 for definitions. Note, that time is given in decimal hours. (e) Short horizontal flight section in the upper part of the mixed phase layer showing the relation of vertical wind speed and classified asphericity of cloud particles. Symbols as in (d). (f) Classification of cloud phase (ice or liquid) from MODIS observations of cloud tops. (g) Mean profile of effective particle radius from ensemble method based on MODIS retrieval data of cloud top effective radius. The black horizontal line indicates the level of largest ice particles.

Atmos. Chem. Phys. Discuss., doi:10.5194/acp-2017-64, 2017
Manuscript under review for journal Atmos. Chem. Phys.
Published: 1 February 2017

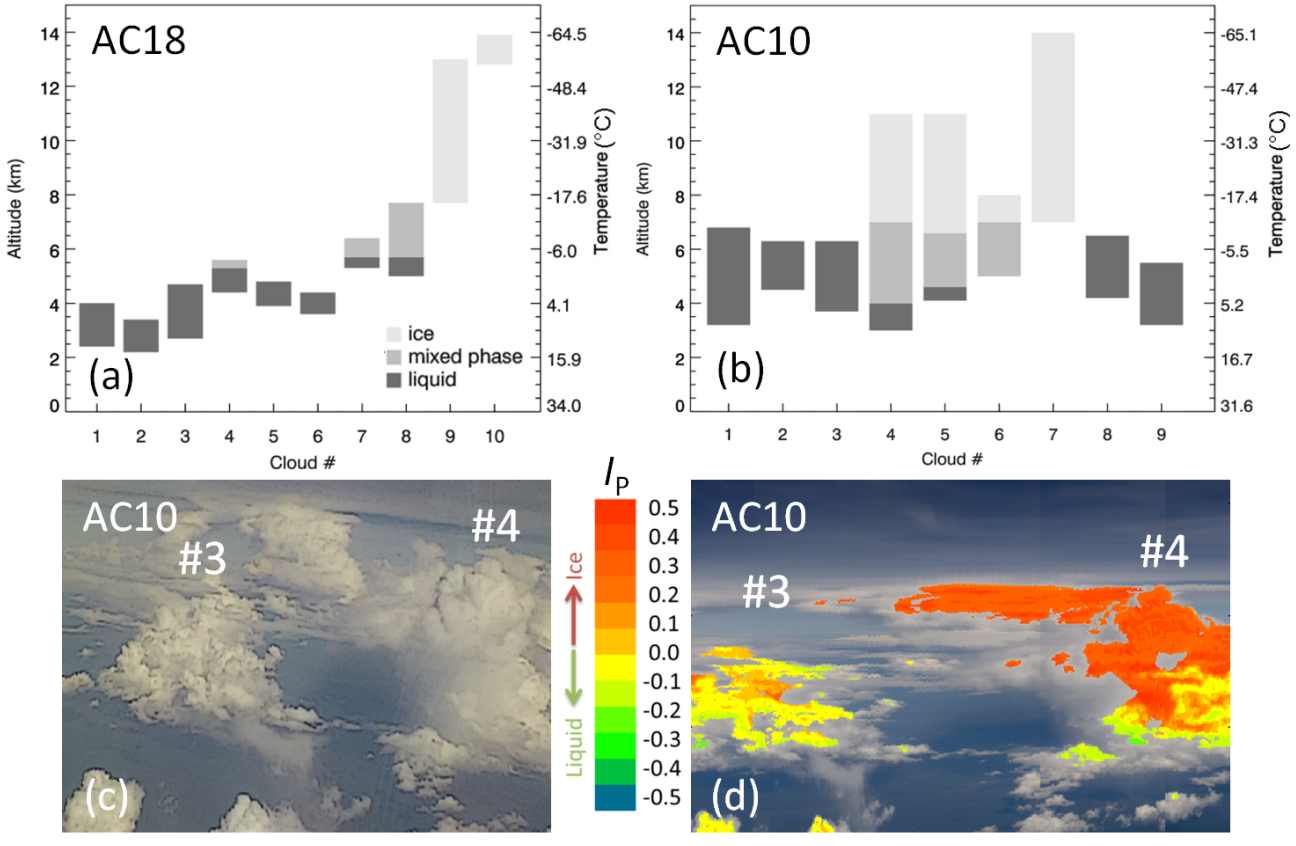

Figure 10. (a) Phase classification of studied clouds based on specMACS observations during flight AC18. (b) Same as (a) but for AC10. (c) GoPro image of cloud scene during AC10. (d) Phase index as derived from specMACS during AC10 for illustrated clouds from (c).